Electronic Supplementary Information

Enforcement of a high-spin ground state for the first 3d heterometallic 12-metallacrown-4 complex

Peter Happ[a,b] and Eva Rentschler*[a]

[a] *Institute of Inorganic and Analytical Chemistry, Johannes Gutenberg University Mainz, Duesbergweg 10-14, D-55128 Mainz, Germany.*

[b] *Graduate School Materials Science in Mainz, Staudinger Weg 9, D-55128 Mainz, Germany*

**Corresponding author*

Eva Rentschler
Institute of Inorganic and Analytical Chemistry
Johannes Gutenberg University Mainz
Duesbergweg 10-14
D-55128 Mainz, Germany

Fax: +49 6131 39 23922
Tel: +49 6131 39 25491
E-mail: rentschler@uni-mainz.de

Experimental Section

All chemicals were reagent grade and were used without further purification.

X-ray diffraction data for the structure analysis were collected from suitable crystals of **1** and **2** on a Bruker SMART 3-circle diffractometer with an APEX II CCD detector and Oxford cooling system using graphite-monochromated Mo-Kα radiation (λ = 0.71073 Å) at -100°C.

Magnetic data were obtained from polycrystalline samples on a Quantum Design MPMS XL SQUID magnetometer equipped with a 7 T magnet. Temperature-dependent magnetic susceptibility data were measured from 2 to 300 K at an applied field of 1 T. Magnetization data were collected in a range between 2 and 10 K for magnetic fields up to 7 T.

C, H and N elemental analyses were carried out on a Foss Heraeus Vario EL at the Institute of Organic Chemistry at the Johannes Gutenberg University Mainz.

Infrared absorption spectra were recorded at room temperature in a range of 400-4000 cm^{-1} on a JASCO FT/IR-4200 spectrometer using KBr pellets.

UV-Vis absorption measurements were performed between 250 and 1000 nm for a 0.002 mM solution of **1** in $CHCl_3$ and between 210 and 1000 nm for a 0.2 and 0.01 mM solution of **2** in MeOH on a JASCO V-570 UV/Vis/NIR spectrophotometer.

Atomic absorption spectroscopy was carried out on a PerkinElmer 5100 ZL spectrometer.

The ^{57}Fe Mössbauer spectrum was recorded in transmission geometry with a $^{57}Co(Rh)$ source kept at room temperature and a conventional spectrometer operating in the constant-acceleration mode. Previously, the powdered sample had been hermetically enclosed in the sample holder made of acryl.

ESI mass spectra were obtained in the positive ion mode from a Waters Q-ToF-ULTIMA 3 with LockSpray source at the Institute of Organic Chemistry at the Johannes Gutenberg University Mainz.

Synthesis

Cu(II)$(DMF)_2Cl_2$[12-$MC_{Fe(III)N(Shi)}$-4]$(DMF)_4$·2DMF (1)

$CuCl_2$ (0.269 g, 2 mmol) and salicylhydroxamic acid (0.153 g, 1 mmol) were dissolved in dimethylformamide (10 ml) and a solution of triethanolamine (0.373 g, 2.5 mmol) in dimethylformamide (10 ml) was added. By addition of a solution of $FeCl_2 \cdot 4H_2O$ (0.199 g, 1 mmol) in dimethylformamide (10 ml), the dark green reaction mixture immediately turned dark red. It was stirred for 16 h and than filtered. Dark red crystals suitable for X-ray diffraction analysis were obtained from the filtrate by slow evaporation after one month.
Yield: 0.126 g (33%).

$(HNEt_3)_2$Cu(II)[12-$MC_{Cu(II)N(Shi)}$-4] (2)

$CuCl_2$ (0.168 g, 1.25 mmol) and salicylhydroxamic acid (0.153 g, 1 mmol) were dissolved in methanol (20 ml) and a solution of triethylamine (0.304 g, 3 mmol) in methanol (10 ml) was added. The dark green reaction mixture was stirred for 16 h and than filtered. Dark green crystals suitable for X-ray diffraction analysis were obtained from the filtrate by slow evaporation after two days.
Yield: 0.185 g (66%).

X-ray Crystallography

A semi-empirical absorption correction of the obtained X-ray diffraction data was performed with MULABS.[1,2] The structures were solved by direct methods with the help of the program SIR97[3] and all non-hydrogen atoms were refined by full-matrix least squares methods on F^2 with anisotropic displacement parameters using SHELXL-97.[4] All carbon bound hydrogen atoms were placed on geometrically calculated positions and refined according to the riding model with an uniform value of U_{iso}. The nitrogen bound hydrogen of the triethylammonium moiety of **2** was located and refined according to the riding model.

Compound	**1**	**2**
Formula	$C_{52}H_{72}C_{l2}CuFe_4N_{12}O_{20}$	$C_{40}H_{48}Cu_5N_6O_{12}$
Formula weight	1543.04	1122.58
T/K	173	173
Wavelength/Å	0.71073	0.71073
Crystal system	Triclinic	Monoclinic
Space group	P-1	P21/c
a/Å	11.7510(5)	9.5697(7)
b/Å	12.8013(5)	18.8080(13)
c/Å	12.8605(5)	11.8032(9)
α/°	96.926(1)	
β/°	111.413 (1)	107.039(2)
γ/°	110.276 (1)	
V/Å^3	1620.39 (11)	2031.2(3)
Z	1	2
δ_{calcd}/gcm^{-3}	1.581	1.835
μ/mm^{-1}	1.359	2.648
Crystal size/mm	0.30 × 0.21 × 0.08	0.47 × 0.45 × 0.24
θ_{max}/°	28.00	28.14
Reflns. collected	35651	19690
Indep. Reflns (Rint)	7811(0.0466)	4967(0.0825)
Data/restrains/parameters	7811/70/478	4967/47/350
Goof on F^2	0.963	1.021
R_1, wR_2 (I>2σ(I))	0.0300 0.0735	0.0343 0.0758
R_1, wR_2 (all data)	0.0444 0.0779	0.0476 0.0795
Largest diff. peak and hole/e Å^{-3}	0.598/-0.354	0.529/-0.547

Table S1 Crystallographic data and refinement parameters for the crystal structures of **1** and **2**.

1		**2**	
Cu1–O1	1.9155(12)	Cu1–O1	1.896(2)
Cu1–O4	1.9114(12)	Cu1–O4	1.8996(19)
Cu1–O9	2.7166(18)	Cu2–O1	1.9032(19)
Fe1–O1	1.9907(13)	Cu2–O2	1.964(2)
Fe1–O2	1.9692(14)	Cu2–O6*	1.871(2)
Fe1–O6*	1.8635(13)	Cu2–N2*	1.926(2)
Fe1–N2*	2.0521(15)	Cu3–O3	1.8999(19)
Fe1–Cl1	2.2473(6)	Cu3–O4	1.907(2)
Fe2–O3	1.8706(13)	Cu3–O5	1.940(2)
Fe2–O4	2.0094(12)	Cu3–N1	1.913(3)
Fe2–O5	1.9976(13)		
Fe2–O7	2.0997(14)	Cu1···Cu2	3.2502(4)
Fe2–O8	2.0964(14)	Cu1···Cu3	3.2421(3)
Fe2–N1	2.0741(15)	Cu2···Cu3	4.5758(5)
		Cu3···Cu2i	4.6057(6)
Fe1···Fe2	4.8905(4)		
Fe1···Cu1	3.4503(3)	N3–H3N	0.91(3)
Fe2···Fe1*	4.8759(4)	N3···O3	2.815(3)
Fe2···Cu1	3.4556(3)	H3N···O3	1.96(3)

Table S2 Selected interatomic distances (Å) in the crystal structures of **1** and **2**.

1		**2**	
Cu1–O1–Fe1	124.07(6)	Cu1–O1–Cu2	117.62 (10)
Cu1–O4–Fe2	123.59(6)	Cu1–O4–Cu3	116.81 (10)
O1–Cu1–O4	90.53(5)	O1–Cu1–O4	91.90(8)
O1–Cu1– O4*	89.47(5)	O1–Cu1–O4*	88.10(8)
O1–Cu1–O9	96.53(5)	O1–Cu2–O2	80.10(8)
O1*–Cu1–O9	83.47(5)	O1–Cu2–N2*	88.77(10)
O4–Cu1–O9	92.68(5)	O2–Cu2– O6*	98.15(8)
O4*–Cu1–O9	87.32(5)	O6*–Cu2–N2*	92.98(11)
O1–Fe1–O2	76.97(5)	O3–Cu3–O5	98.87(8)
O1–Fe1–N2*	83.51(5)	O3–Cu3–N1	93.05(9)
O1–Fe1–Cl1	105.35(4)	O4–Cu3–O5	81.20(8)
O2–Fe1–O6*	95.39(6)	O4–Cu3–N1	91.52(10)
O2–Fe1–Cl1	104.03(5)		
O6*–Fe1–N2*	86.81(6)		
O6*–Fe1–Cl1	109.41(5)		
N2*–Fe1–Cl1	104.62(5)		
O3–Fe2–O5	112.06(6)		
O3–Fe2–O7	88.50(6)		
O3–Fe2–O8	90.90(6)		
O3–Fe2–N1	87.18(6)		
O4–Fe2–O5	77.48(5)		
O4–Fe2–O7	89.52(5)		
O4–Fe2–O8	92.11(6)		
O4–Fe2–N1	83.49(5)		
O5–Fe2–O7	89.03(6)		
O5–Fe2–O8	85.35(6)		
O7–Fe2– N1	95.79(6)		
O8–Fe2–N1	90.47(6)		

Table S3 Selected bond angles (°) in the crystal structures of **1** and **2**.

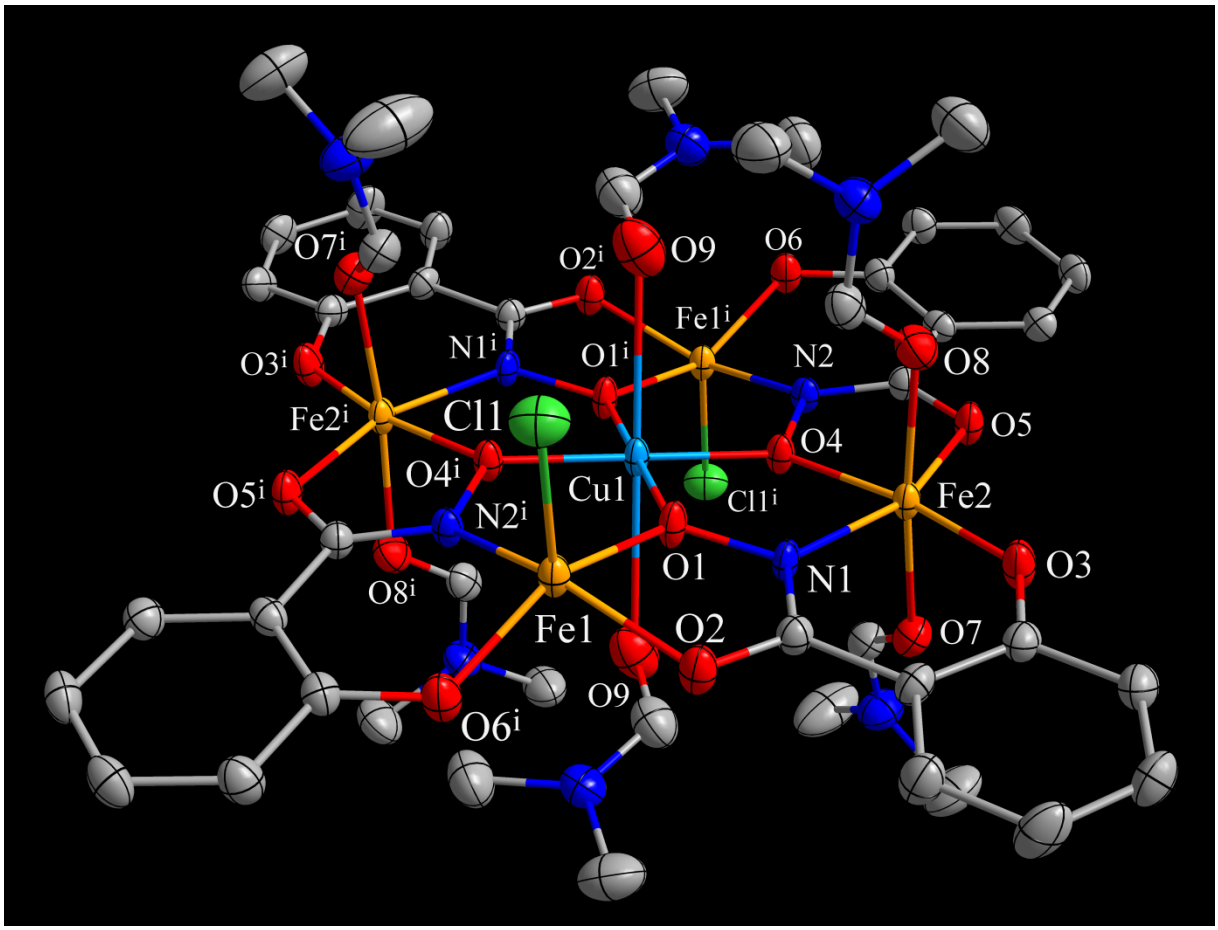

Figure S1 Molecular structure of Cu(II)$(DMF)_2Cl_2$[12-$MC_{Fe(III)N(Shi)}$-4]$(DMF)_4$ in crystals of **1** with numbering scheme and thermal ellipsoids at 50% probability level; colour scheme: light blue - Cu(II), yellow - Fe(III), green - Cl, red - O, dark blue - N, grey - C.

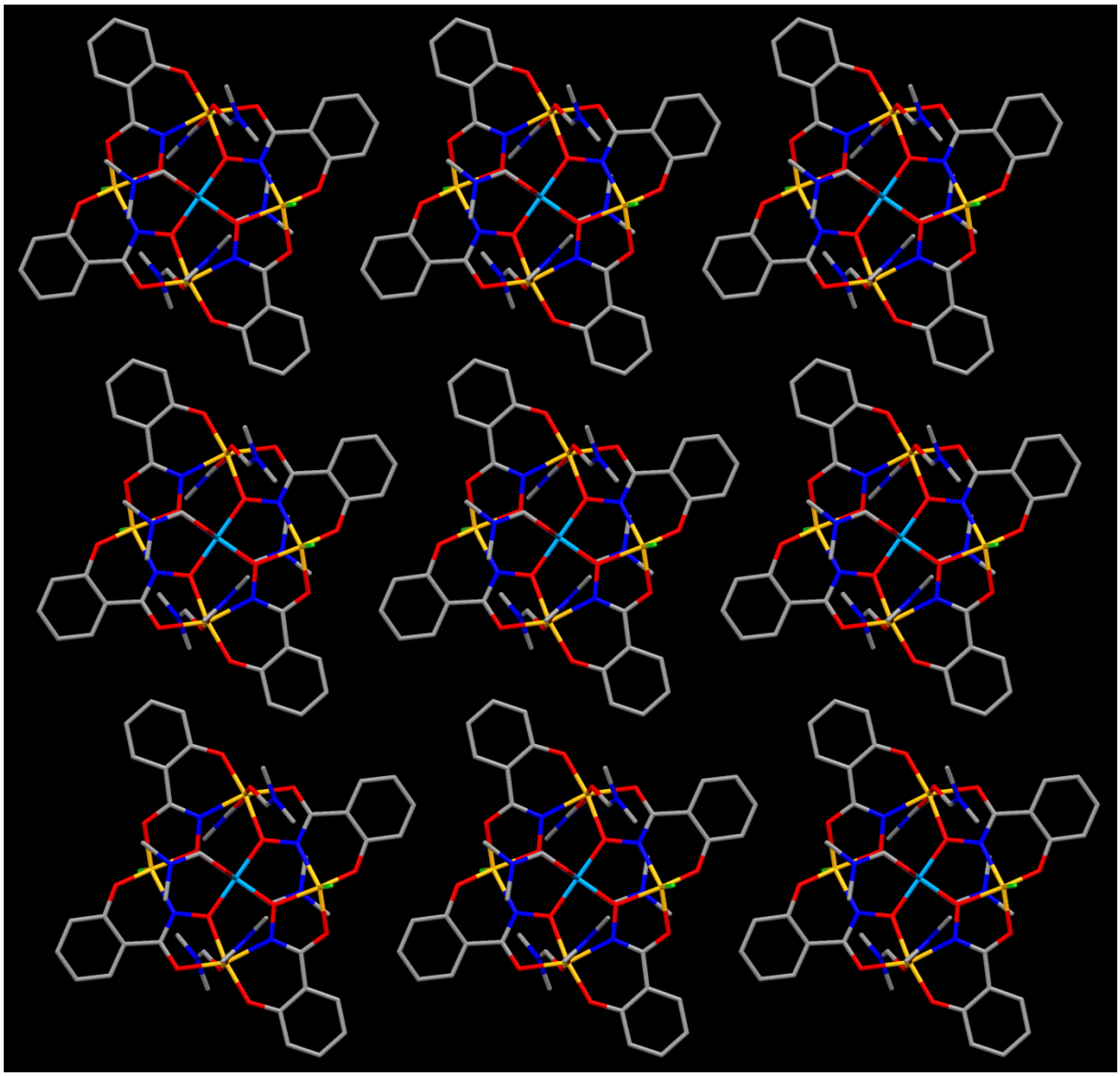

Figure S2 packing of the Cu(II)$(DMF)_2Cl_2$[12-$MC_{Fe(III)N(Shi)}$-4]$(DMF)_4$ units in the plane spanned by the a+b and a+c vector in the crystal structure of **1**; colour scheme: light blue - Cu(II), yellow - Fe(III), green - Cl, red - O, dark blue - N, grey - C.

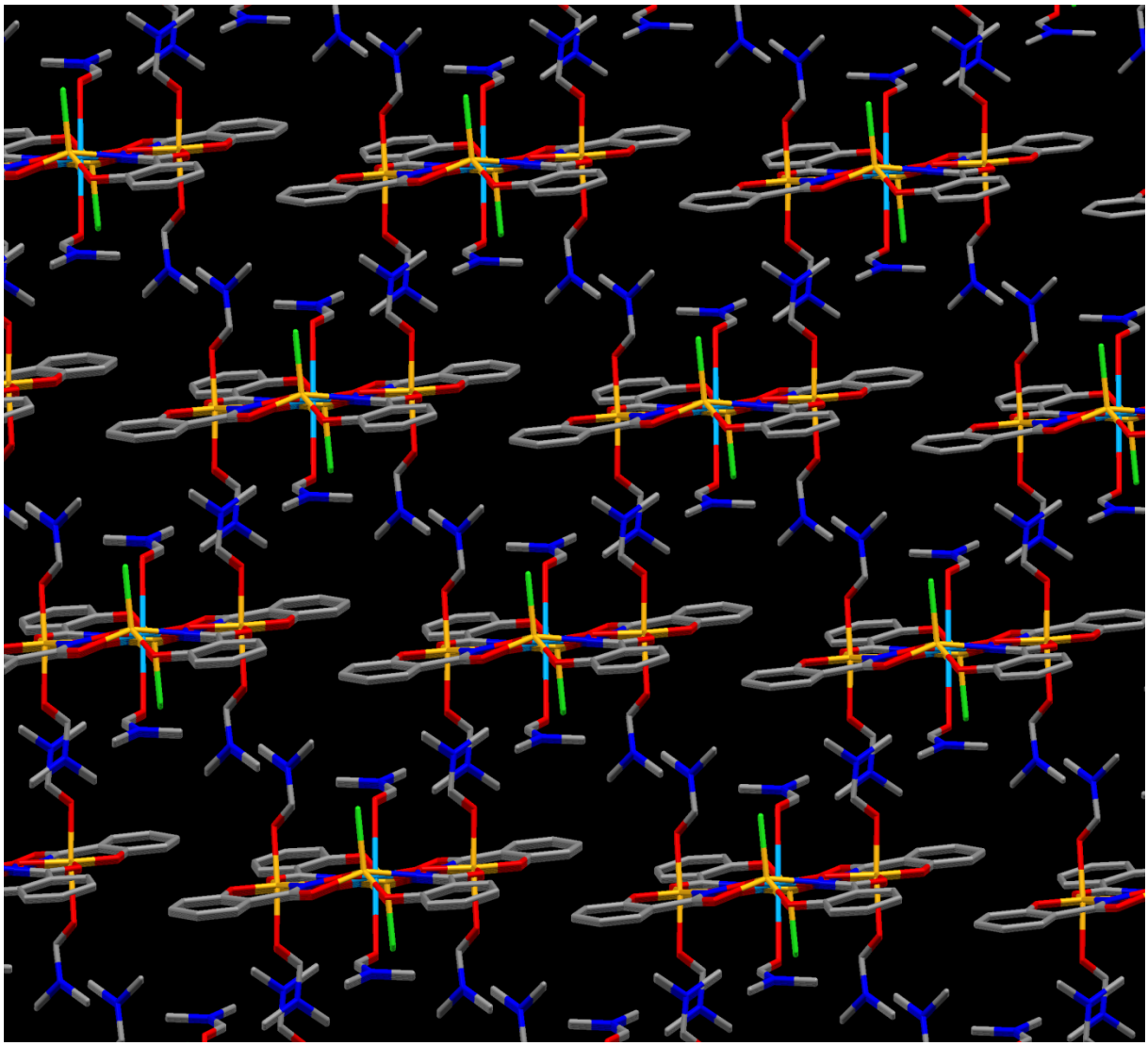

Figure S3 Stacking of the layers in the crystal structure of **1**; colour scheme: light blue - Cu(II), yellow - Fe(III), green - Cl, red - O, dark blue - N, grey - C.

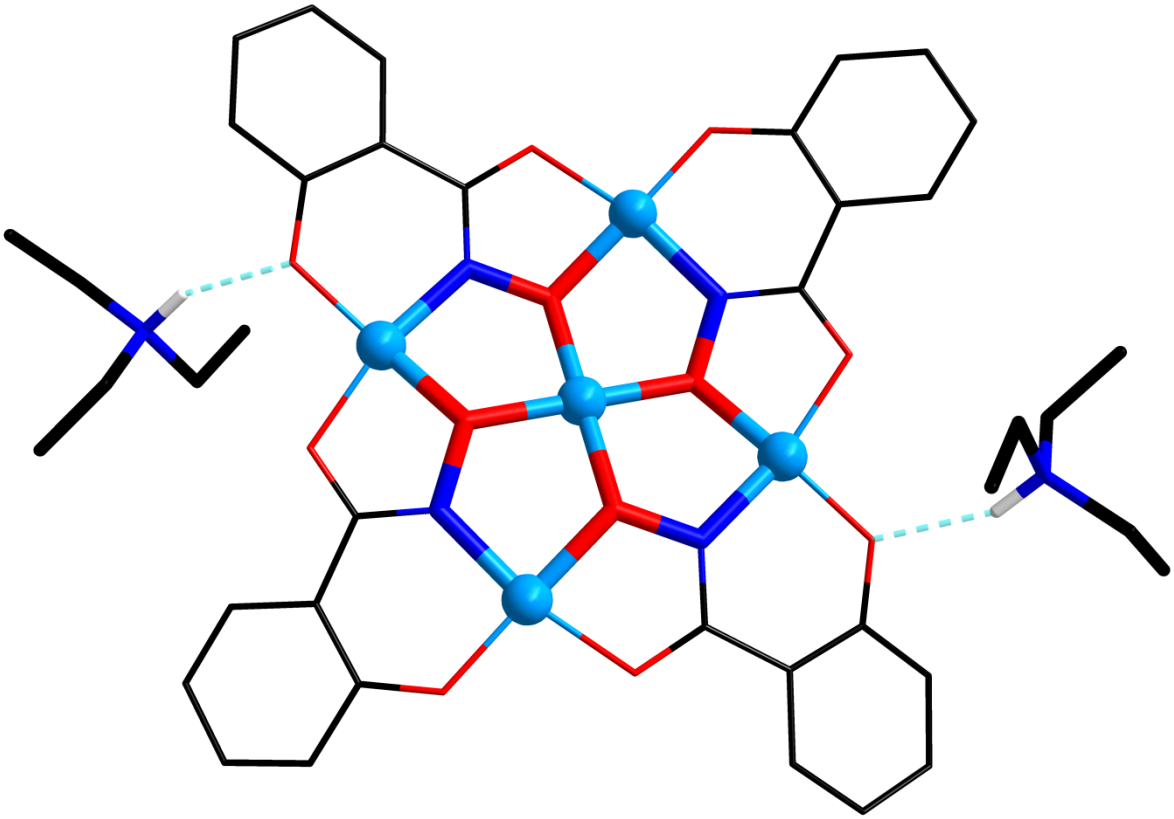

Figure S4 Molecular structure of $(HNEt_3)_2Cu(II)[12\text{-}MC_{Cu(II)N(Shi)}\text{-}4]$ in crystals of **2**; colour scheme: light blue - Cu(II), red - O, dark blue - N, grey - C.

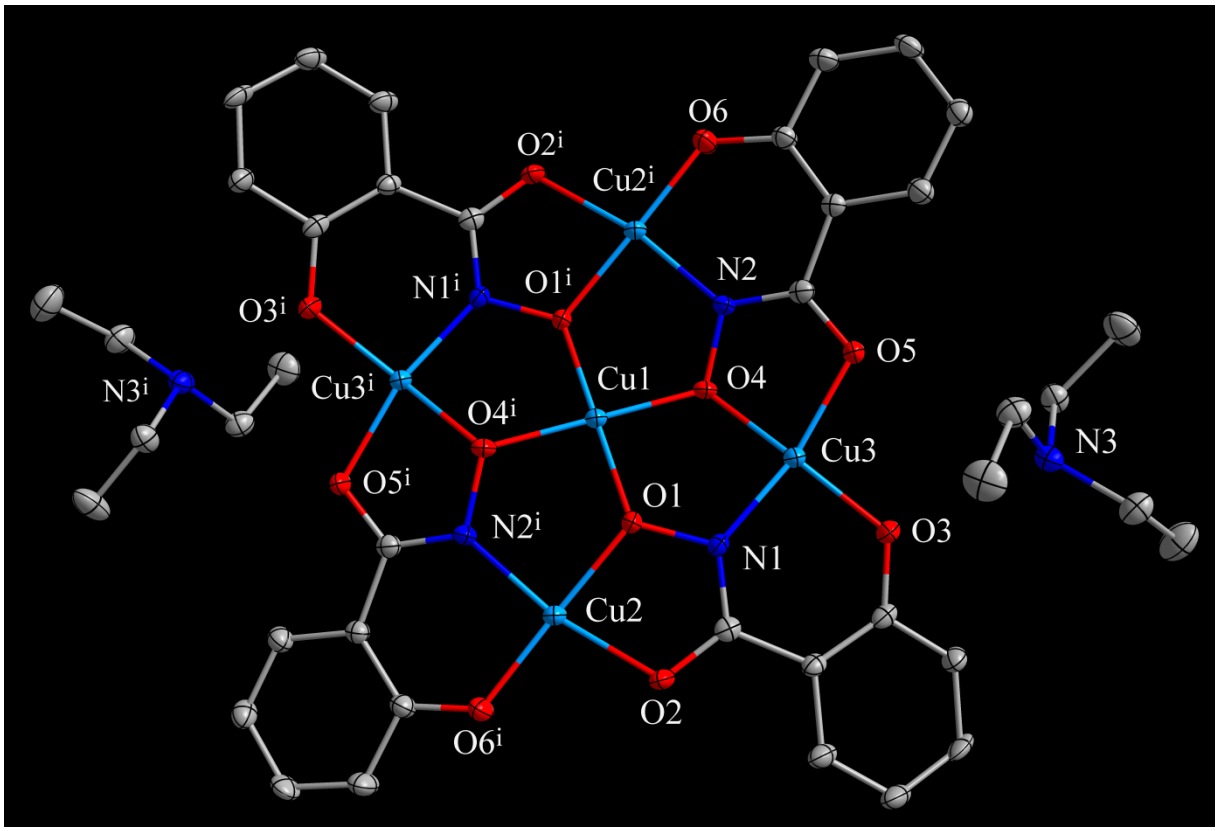

Figure S5 Molecular structure of $(HNEt_3)_2Cu(II)[12\text{-}MC_{Cu(II)N(Shi)}\text{-}4]$ in crystals of **2** with numbering scheme and thermal ellipsoids at 50% probability level; colour scheme: light blue - Cu(II), red - O, dark blue - N, grey - C.

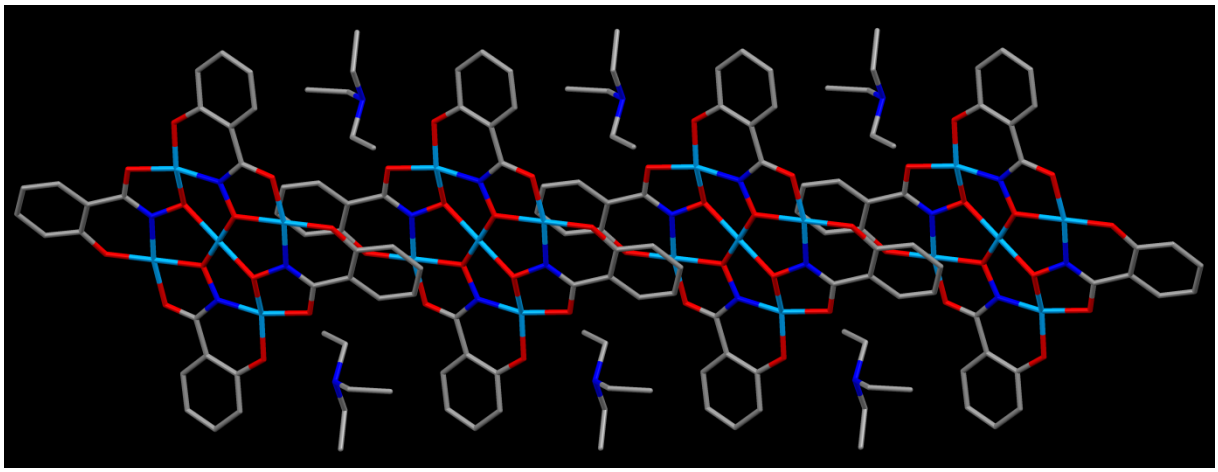

Figure S6 Packing of the $(HNEt_3)_2Cu(II)[12\text{-}MC_{Cu(II)N(Shi)}\text{-}4]$ units towards chains along the a axis in the crystal structure of **2**; view on the ac plane in b direction; colour scheme: light blue - Cu(II), red - O, dark blue - N, grey - C.

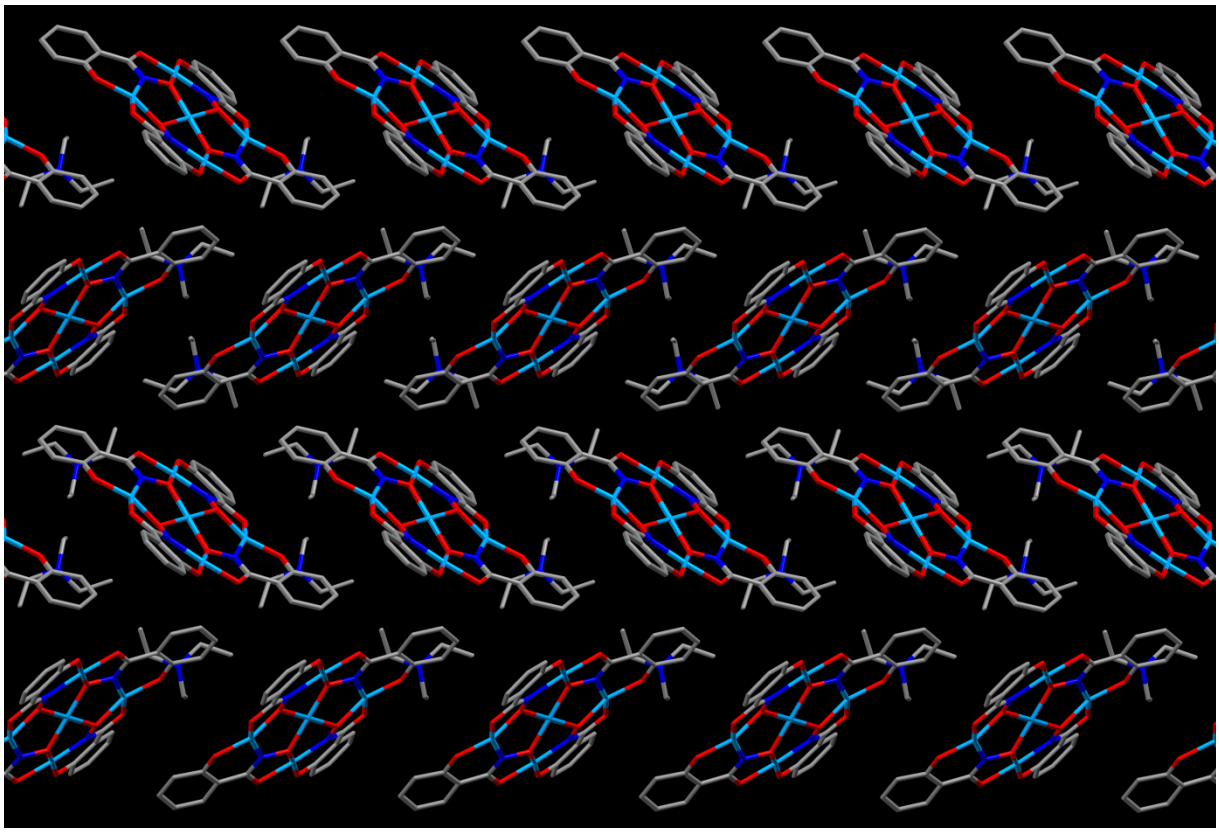

Figure S7 Packing of the chains towards layers along the c axis and stacking of these layers in b direction in the crystal structure of **2**; view on the bc plane along the a direction; colour scheme: light blue - Cu(II), red - O, dark blue - N, grey - C.

Elemental Analysis

1: Found: C, 40.48; H, 4.60; N, 10.96. Calc. for $C_{52}H_{72}Cl_2Cu_1Fe_4N_{12}O_{20}$: C, 40.48; H, 4.70; N, 10.89%

2: Found: C, 42.92; H, 4.47; N, 7.35. Calc. for $C_{40}H_{48}Cu_5N_6O_{12}$: C, 42.80; H, 4.31; N, 7.49%

Infrared Absorption Spectroscopy

1: ν_{max}/cm^{-1}

3146br, 3059w, 2929m, 2864w, 2806w, 1647vs ($\nu(C=O)_{DMF}$), 1595s ($\nu(C=N)_{Shi}$), 1561s, 1492vs, 1427s, 1383s, 1316s, 1258s ($\nu(N-O)_{Shi}$), 1156m, 1145w, 1117w, 1100m, 1063w, 1034w, 1010m, 935s, 865s, 774w, 758s, 684s, 649s, 634w, 578w, 541w, 503w, 463m

2: ν_{max}/cm^{-1}

3136w, 3025w, 2980m, 2942w, 2882w, 2737w, 2678w, 1597s ($\nu(C=N)_{Shi}$), 1565vs, 1523s, 1466m, 1433m, 1386s, 1321s, 1253s ($\nu(N-O)_{Shi}$), 1175w, 1152m, 1093m, 1065w, 1029m, 1020m, 943s, 852m, 795w, 755s, 688s, 654s, 580m, 545w, 509w, 475m, 454w, 424m

The assignment of characteristic bands was performed via a comparison with reported data for similar salicylhydroxamic acid based metallacrowns.[5-10]

UV-Vis Absorption Spectroscopy

1: $\lambda_{max}(CHCl_3)$/nm 296 (ε/dm³ mol^{-1} cm^{-1} 48200), 472 (18400)

2: λ_{max}(MeOH)/nm 216 (ε/dm³ mol^{-1} cm^{-1} 110000), 236 (85000), 318 (29200), 616 (711)

The band at 616 nm for **2** represents a copper centred d-d transition[11] whereas the light absorption by **1** at 472 nm is characteristic for a ligand-to-metal charge-transfer (LMCT) in hydroxamate iron complexes.[12-15] By comparison with the measured absorption maxima of the free main ligand salicylhydroxamic acid at 300 and 236 nm, the bands at 318, 236 nm of **2** and 296 nm of **1** can be assigned to excitations within the delocalized π-system of the coordinated hydroximate ligand.

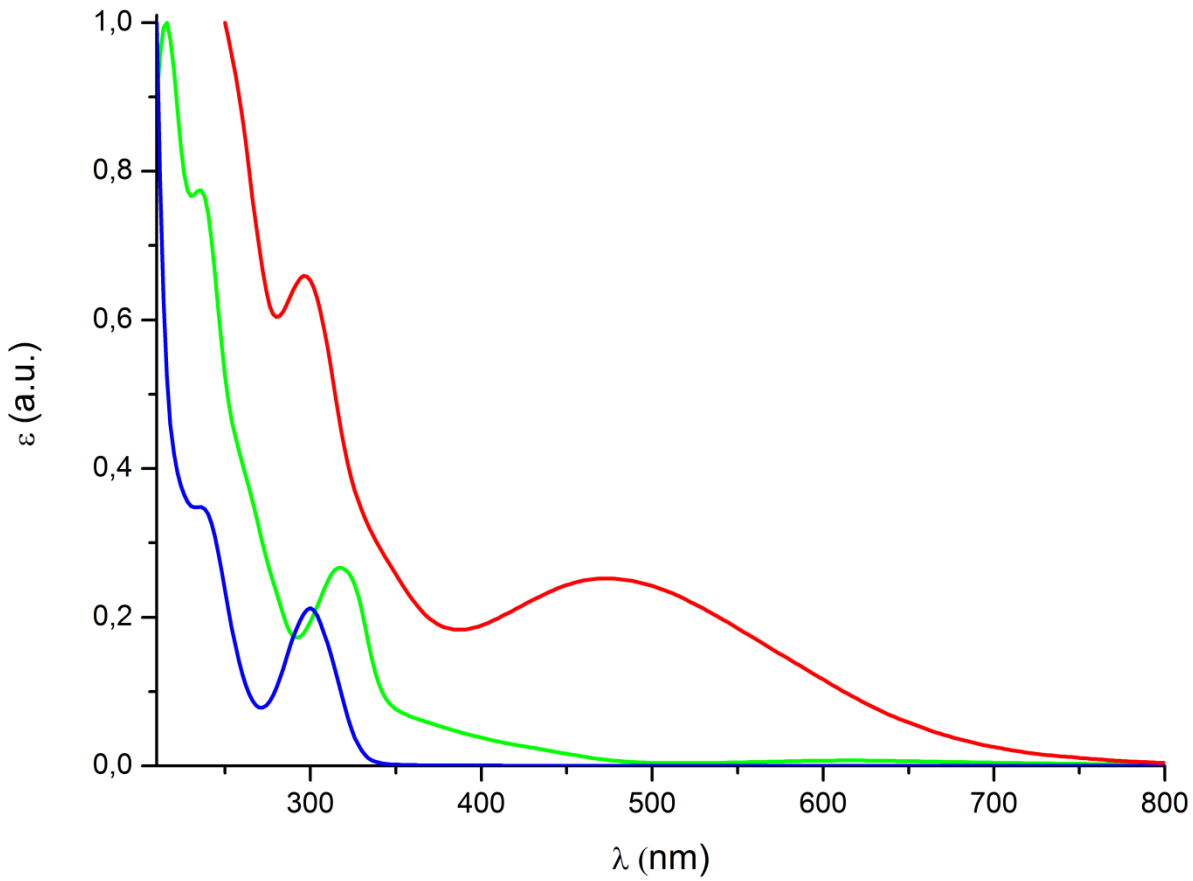

Figure S8 Normalized UV-Vis spectra of **1** in $CHCl_3$ (red), **2** in MeOH (green) and H_3Shi in MeOH (blue).

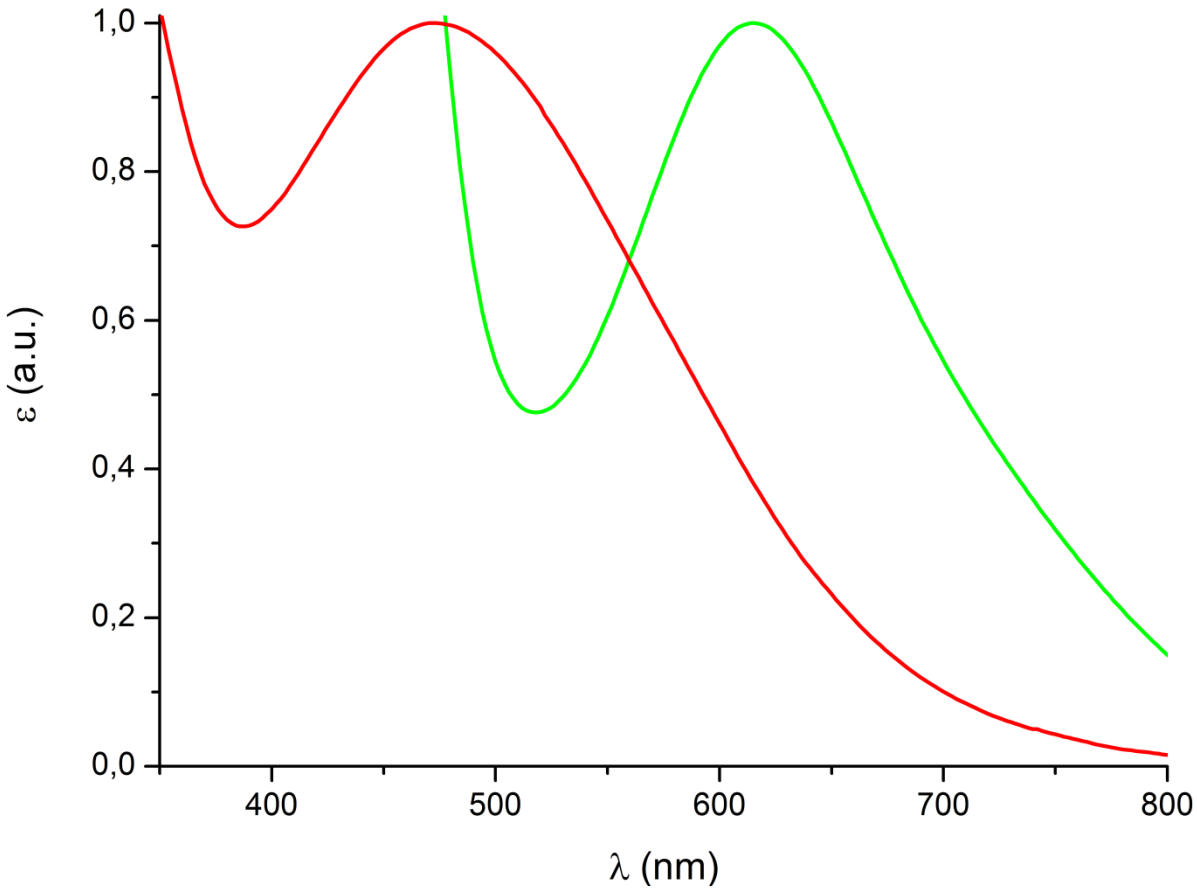

Figure S9 Normalized extract of the UV-Vis spectra of **1** in $CHCl_3$ (red) and **2** in MeOH (green).

Atomic Absorption Spectroscopy

1: Found: ratio Cu:Fe, 1:4.15. Calc. for $C_{52}H_{72}Cl_2Cu_1Fe_4N_{12}O_{20}$: ratio Cu:Fe, 1:4.

Mößbauer Spectroscopy

The evaluation of the ^{57}Fe Mößbauer spectrum was performed with the help of the RECOIL 1.03 fit routine.[16] The optimized reasonable fit results of an applied two-site model for the isomer shift (δ_{IS}), quadrupole splitting (ΔE_Q), Lorentzian line width (Γ) and the area ratio (A) are given below.

1: doublet 1: δ_{IS} 0.4343 mm s^{-1}, ΔE_Q 1.816 mm s^{-1}, Γ 0.179 mm s^{-1}, A 49.8%
doublet 2: δ_{IS} 0.3336 mm s^{-1}, ΔE_Q 1.108 mm s^{-1}, Γ 0.181 mm s^{-1}, A 50.2%

The spectrum exhibits the presence of two distinct iron species, which are comprised in the compound with same quantity and both reveal typical values of the isomer shift for high-spin Fe(III) ions. Furthermore, the quite distinct quadrupol splittings match the inhomogeneous arrangement of donor atoms in the two distinguishable coordination spheres. Hence, the wider doublet might moreover be attributed to the five-fold coordinated iron ion with the apical chloro ligand.

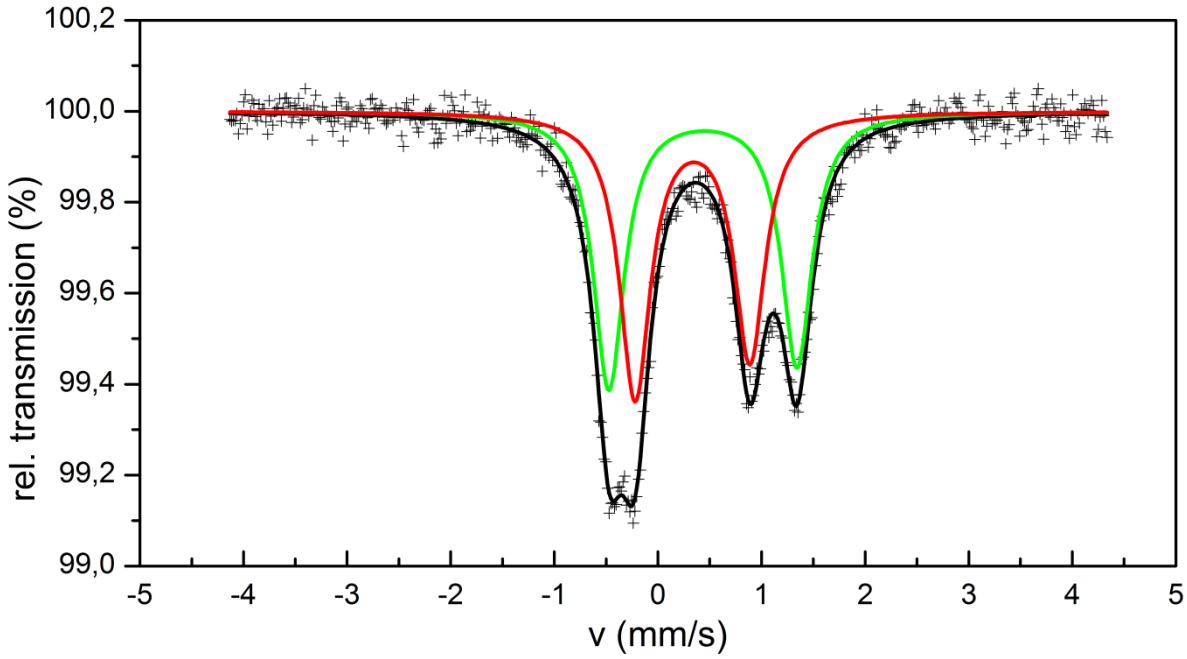

Figure S10 Mößbauer spectrum of **1**; solid lines represent the result of the entire fit (black), the fit for doublet 1 (green) and doublet 2 (red).

ESI Mass Spectrometry

1: m/z(DMF:MeCN/1:1)

1126 $\{(Cu(II)(Cl)_2[12\text{-}MC_{Fe(III)N(Shi)}\text{-}4](DMF)_2)Na\}^+$

1141 $\{Cu(II)Cl[12\text{-}MC_{Fe(III)N(Shi)}\text{-}4](DMF)_3\}^+$

2: m/z(MeCN)

920 $\{(Cu(II)[12\text{-}MC_{Cu(II)N(Shi)}\text{-}4])H_3\}^+$

1021 $\{(Cu(II)[12\text{-}MC_{Cu(II)N(Shi)}\text{-}4])(HNEt_3)H_2\}^+$

1122 $\{(Cu(II)[12\text{-}MC_{Cu(II)N(Shi)}\text{-}4])(HNEt_3)_2H\}^+$

1225 $\{(Cu(II)[12\text{-}MC_{Cu(II)N(Shi)}\text{-}4])(HNEt_3)_3\}^+$

1583 $\{(Cu(II)[12\text{-}MC_{Cu(II)N(Shi)}\text{-}4])_3(HNEt_3)_4H_4\}^{2+}$

1942 $\{(Cu(II)[12\text{-}MC_{Cu(II)N(Shi)}\text{-}4])_2(HNEt_3)H_4\}^+$

2043 $\{(Cu(II)[12\text{-}MC_{Cu(II)N(Shi)}\text{-}4])_2(HNEt_3)_2H_3\}^+$

2: m/z(MeOH)

942 $\{(Cu(II)[12\text{-}MC_{Cu(II)N(Shi)}\text{-}4])NaH_2\}^+$

964 $\{(Cu(II)[12\text{-}MC_{Cu(II)N(Shi)}\text{-}4])Na_2H\}^+$

1021 $\{(Cu(II)[12\text{-}MC_{Cu(II)N(Shi)}\text{-}4])(HNEt_3)H_2\}^+$

1043 $\{(Cu(II)[12\text{-}MC_{Cu(II)N(Shi)}\text{-}4])(HNEt_3)NaH\}^+$

1122 $\{(Cu(II)[12\text{-}MC_{Cu(II)N(Shi)}\text{-}4])(HNEt_3)_2H\}^+$

1583 $\{(Cu(II)[12\text{-}MC_{Cu(II)N(Shi)}\text{-}4])(HNEt_3)_4H_4\}^{2+}$

Magnetism

In the course of the data processing of all magnetic measurements, diamagnetic corrections were applied for the holder as well as for the intrinsic contributions of atoms and moieties with the help of Pascal's constants.[17] The fitting of the temperature-dependent susceptibility data was performed with the help of the program CLUMAG[18] using the χT vs. T plot of the measured data above 10 K. Model calculations and the simulation of the magnetization data of **1** were carried out via the software package FIT-MART.[19]

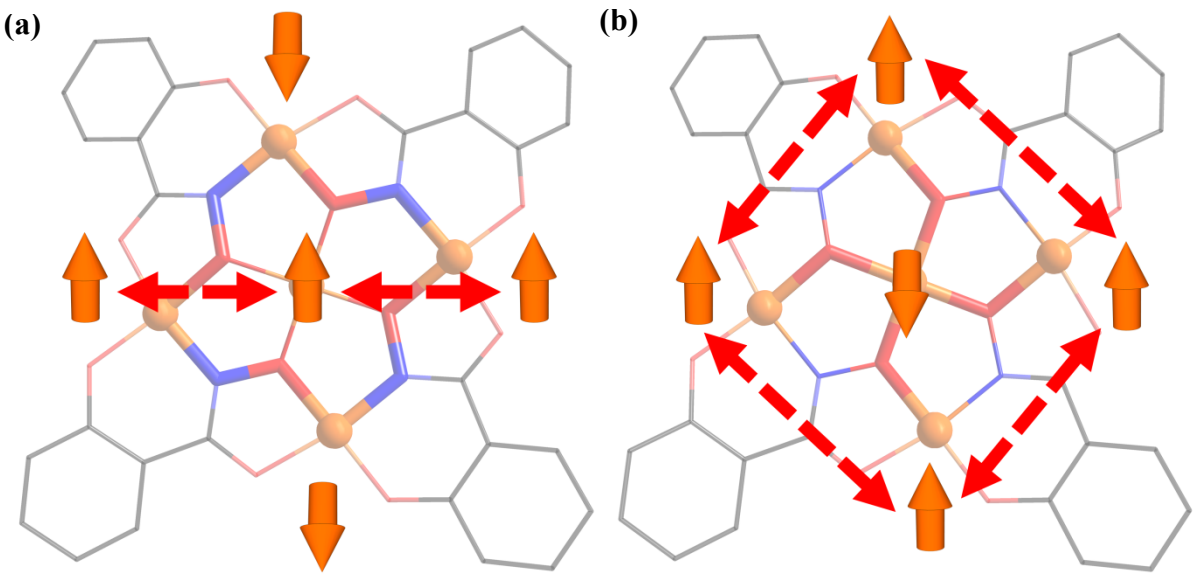

Figure S11 Illustrative visualization of the energetic preference of a low-spin ground state in 12-MC-4 complexes due to the intrinsic magnetic connectivity by a comparison of both extreme cases of alternating (a) and parallel (b) spin alignment in the ring; assuming a homometallic metallacrown with all spin centres S = ½ and identically antiferromagnetic coupling constants J_1 and J_2, every parallel alignment of spins (red arrows) means an energetic penalty relative to an antiparallel orientation; the preference of the low-spin state can be illustrated by a simple counting of the penalties for the alternating (2) and parallel (4) spin alignment in the ring.

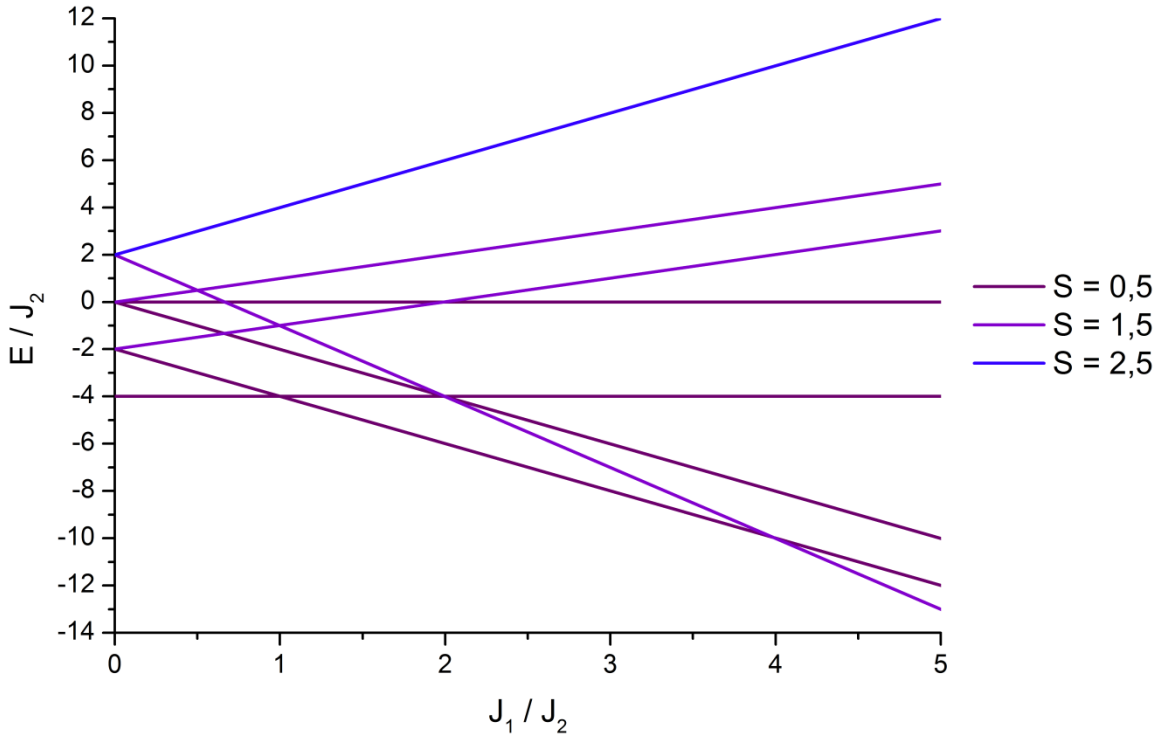

Figure S12 Coupling constants ratio-dependent normalized energy level diagram of a square magnetic model for a generalized Cu(II)[12-$MC_{Cu(II)N(Shi)}$-4]$^{2-}$ complex with radial (J_1) and tangential (J_2) antiferromagnetic interactions according to an isotropic Heisenberg Hamiltonian.

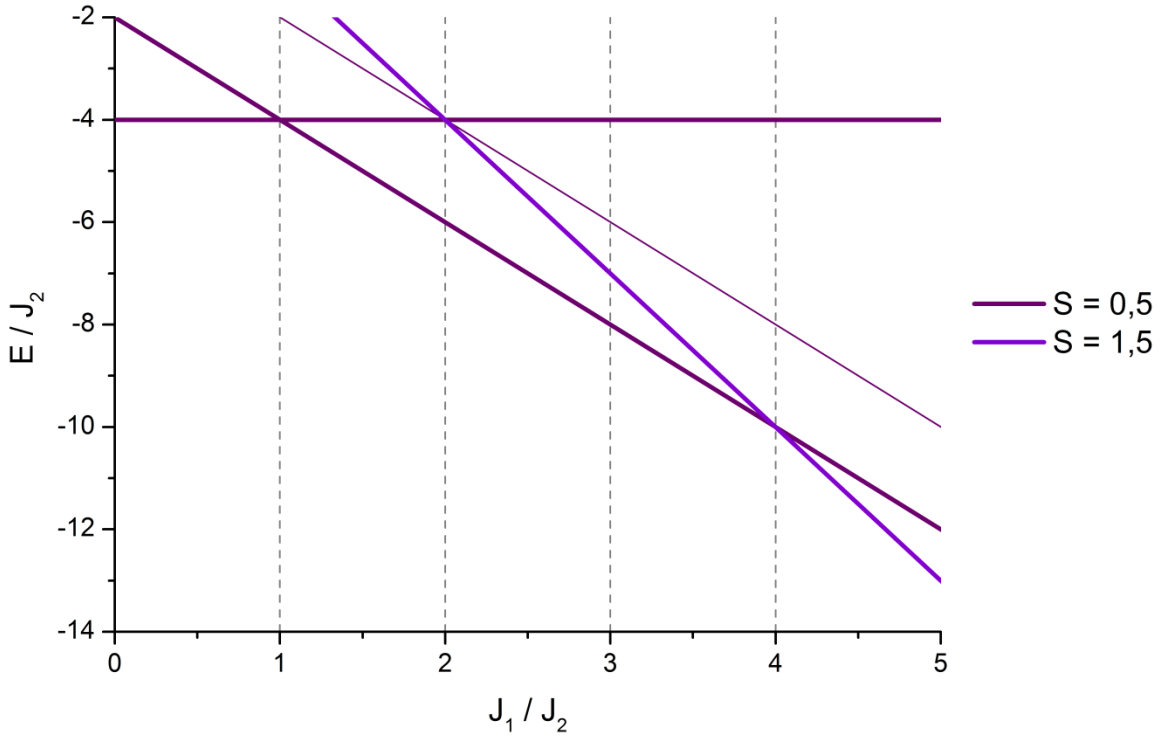

Figure S13 Coupling constants ratio-dependent normalized energy level diagram of a square magnetic model for a generalized Cu(II)[12-$MC_{Cu(II)N(Shi)}$-4]$^{2-}$ complex with radial (J_1) and tangential (J_2) antiferromagnetic interactions according to an isotropic Heisenberg Hamiltonian with special focus on the spin ground states; occurring spin ground states are highlighted.

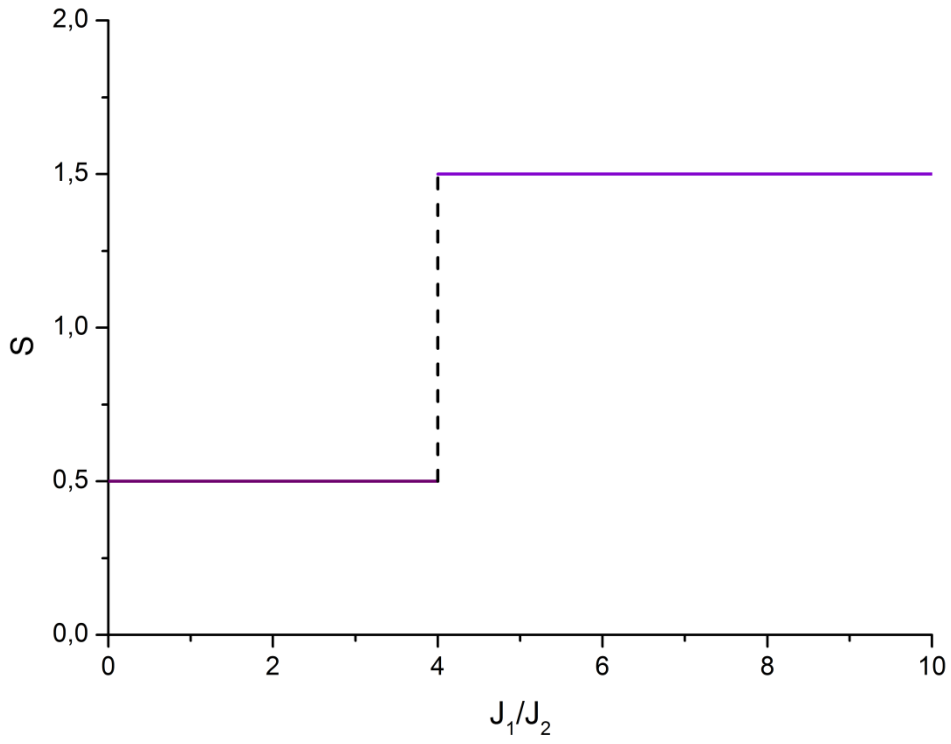

Figure S14 Coupling constants ratio dependence of the value of the spin ground state of a square magnetic model for a generalized Cu(II)[12-$MC_{Cu(II)N(Shi)}$-4]$^{2-}$ complex with radial (J_1) and tangential (J_2) antiferromagnetic interactions according to an isotropic Heisenberg Hamiltonian.

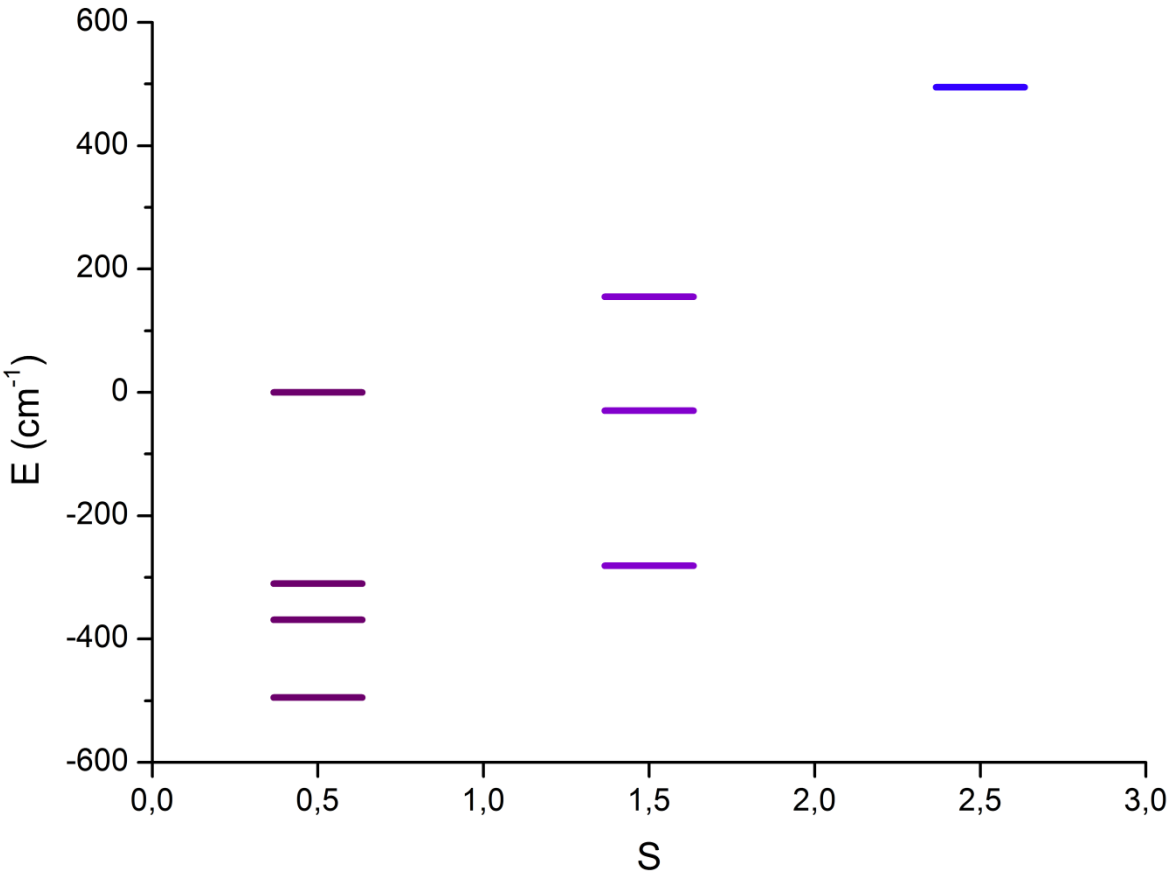

Figure S15 Energy level diagram of the spin states of the Cu(II)[12-$MC_{Cu(II)N(Shi)}$-4]$^{2-}$ complex in **2** according to the best fit result of the temperature dependence of the $\chi_M T$ product ($\chi_M T$ vs. T plot; Fig. 4) for a square magnetic model using an isotropic Heisenberg Hamiltonian.

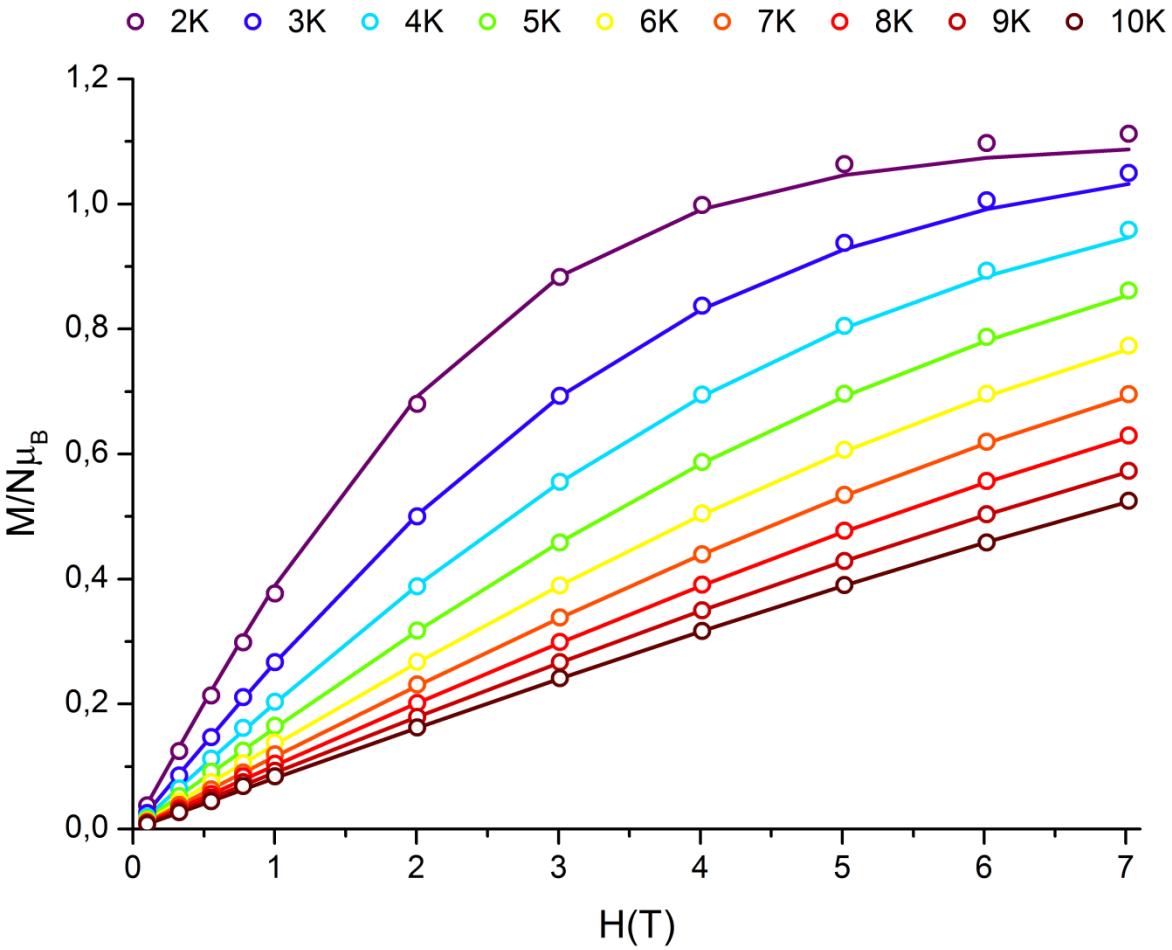

Figure S16 Field dependence of the reduced magnetization ($M/N\mu_B$ vs. H plot) of **2** for different temperatures between 2 and 10 K; solid lines represent simulations according to the Broillouin function for an isolated S = ½ ground state and a g-factor of g = 2.2.

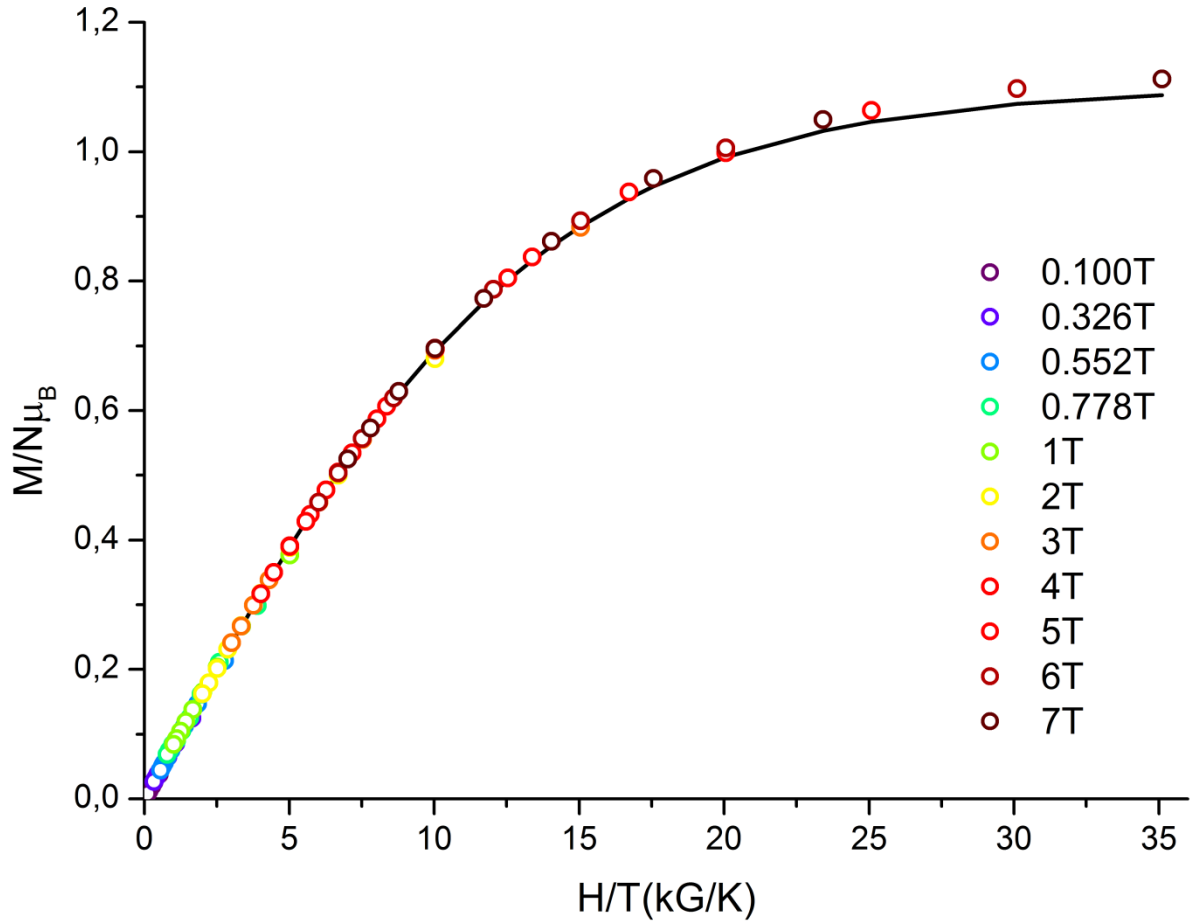

Figure S17 Field-temperature ratio dependence of the reduced magnetization ($M/N\mu_B$ vs. H/T plot) of **2** at temperatures between 2 and 10 K for applied magnetic fields from 0.1 to 7 T; the solid line represents the simulated master curve according to the Broillouin function for an isolated S = ½ spin ground state and a g-factor of g = 2.2.

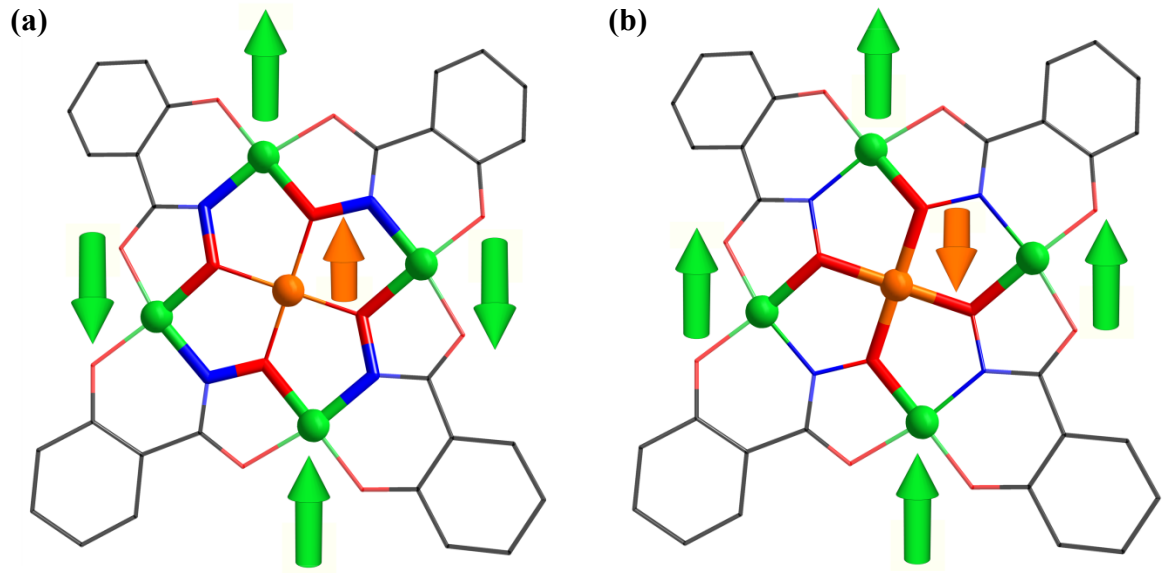

Figure S18 Schematic drawing of an alternating and parallel spin alignment of the cyclic host of a 12-MC-4 metallacrown in the ground state as extreme cases of dominantly tangential (a) and radial (b) antiferromagnetic interactions; the respective superior coupling pathways are graphically highlighted.

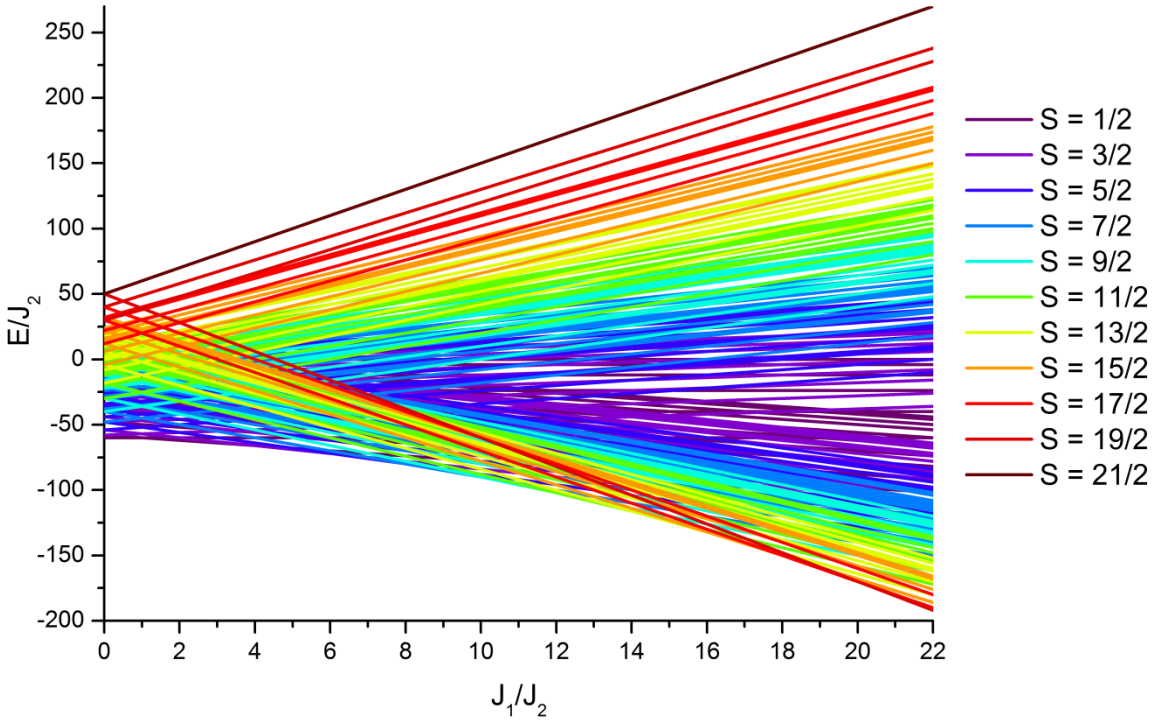

Figure S19 Coupling constants ratio-dependent normalized energy level diagram of a square magnetic model for a generalized Cu(II)[12-$MC_{Fe(III)N(Shi)}$-4] complex with radial (J_1) and tangential (J_2) antiferromagnetic interactions according to an isotropic Heisenberg Hamiltonian.

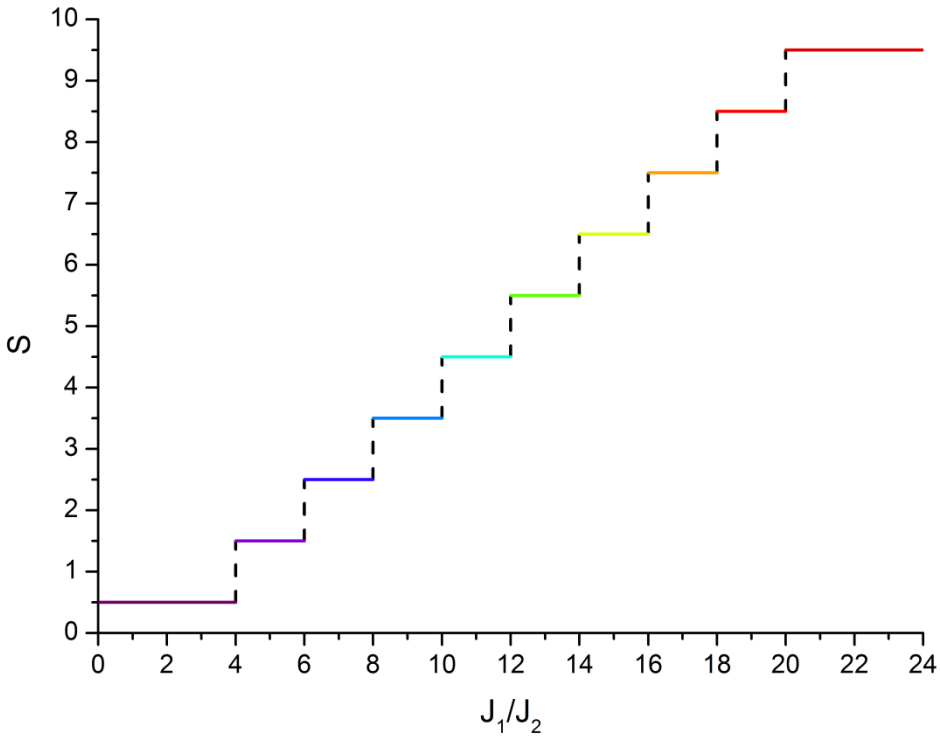

Figure S20 Coupling constants ratio dependence of the value of the spin ground state of a square magnetic model for a generalized Cu(II)[12-$MC_{Fe(III)N(Shi)}$-4]$^{2-}$ complex with radial (J_1) and tangential (J_2) antiferromagnetic interactions according to an isotropic Heisenberg Hamiltonian.

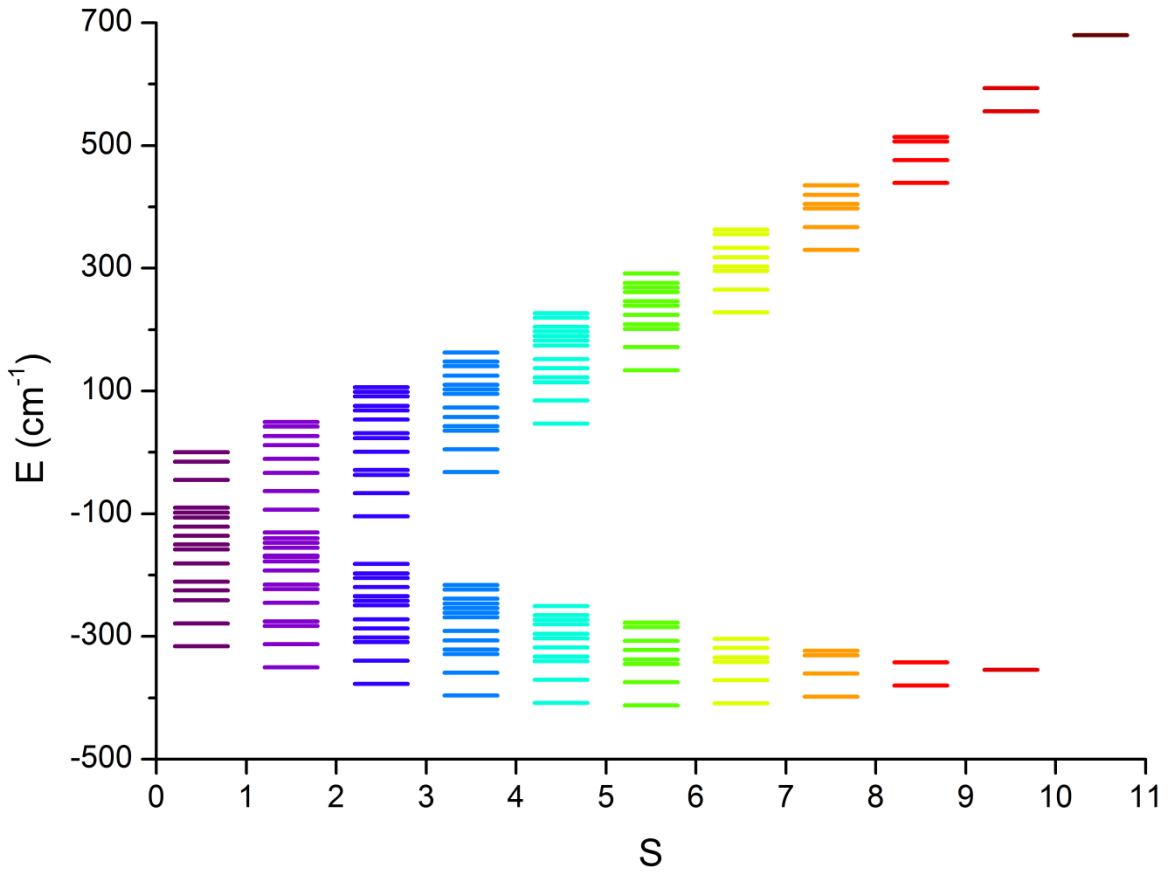

Figure S21 Energy level diagram of the spin states of the $Cu(DMF)_2Cl_2[12\text{-}MC_{Fe(III)N(Shi)}\text{-}4](DMF)_4$ complex in **1** according to the best fit result of the temperature dependence of the $\chi_M T$ product ($\chi_M T$ vs. T plot; Fig. 5) for a square magnetic model using an isotropic Heisenberg Hamiltonian.

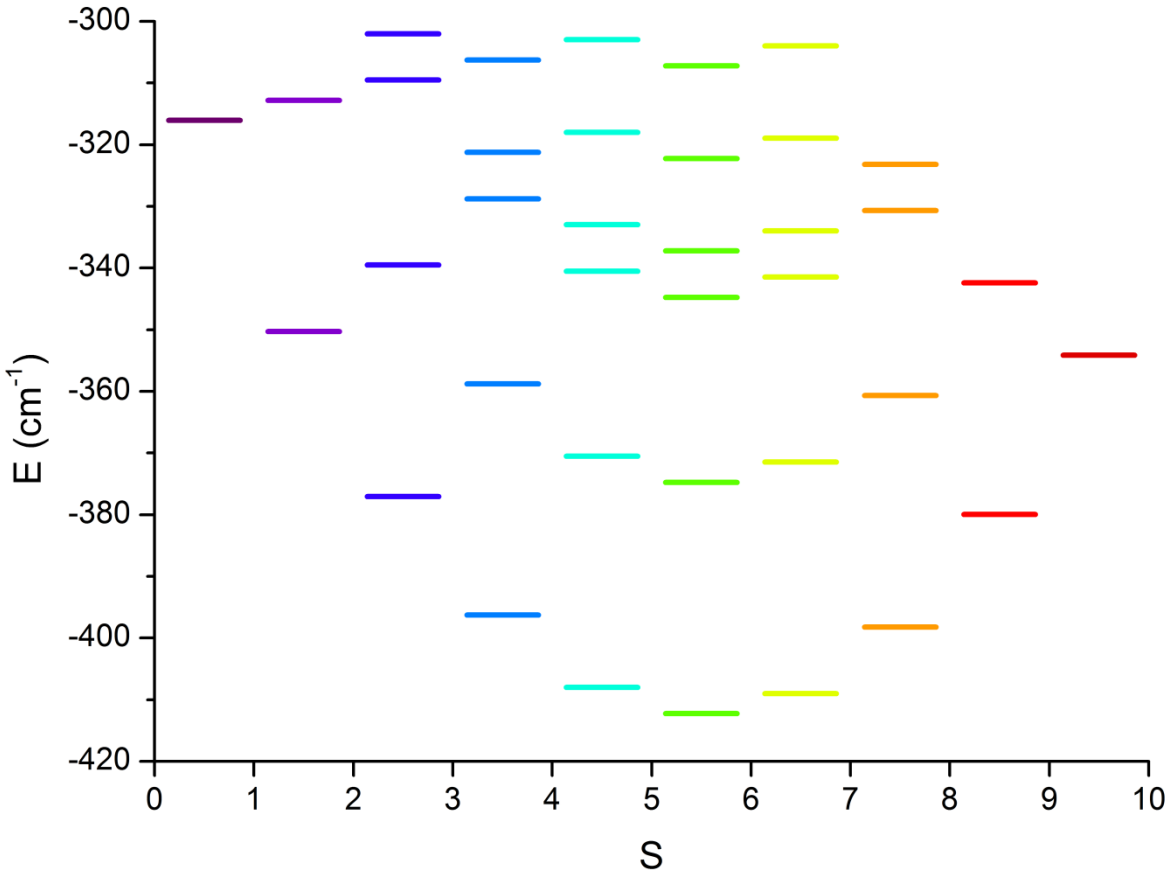

Figure S22 Energy level diagram of the spin states of the Cu(II)$(DMF)_2Cl_2$[12-$MC_{Fe(III)N(Shi)}$-4]$(DMF)_4$ complex in **1** according to the best fit result of the temperature dependence of the $\chi_M T$ product ($\chi_M T$ vs. T plot; Fig. 5) for a square magnetic model using an isotropic Heisenberg Hamiltonian with focus on the lowest lying states.

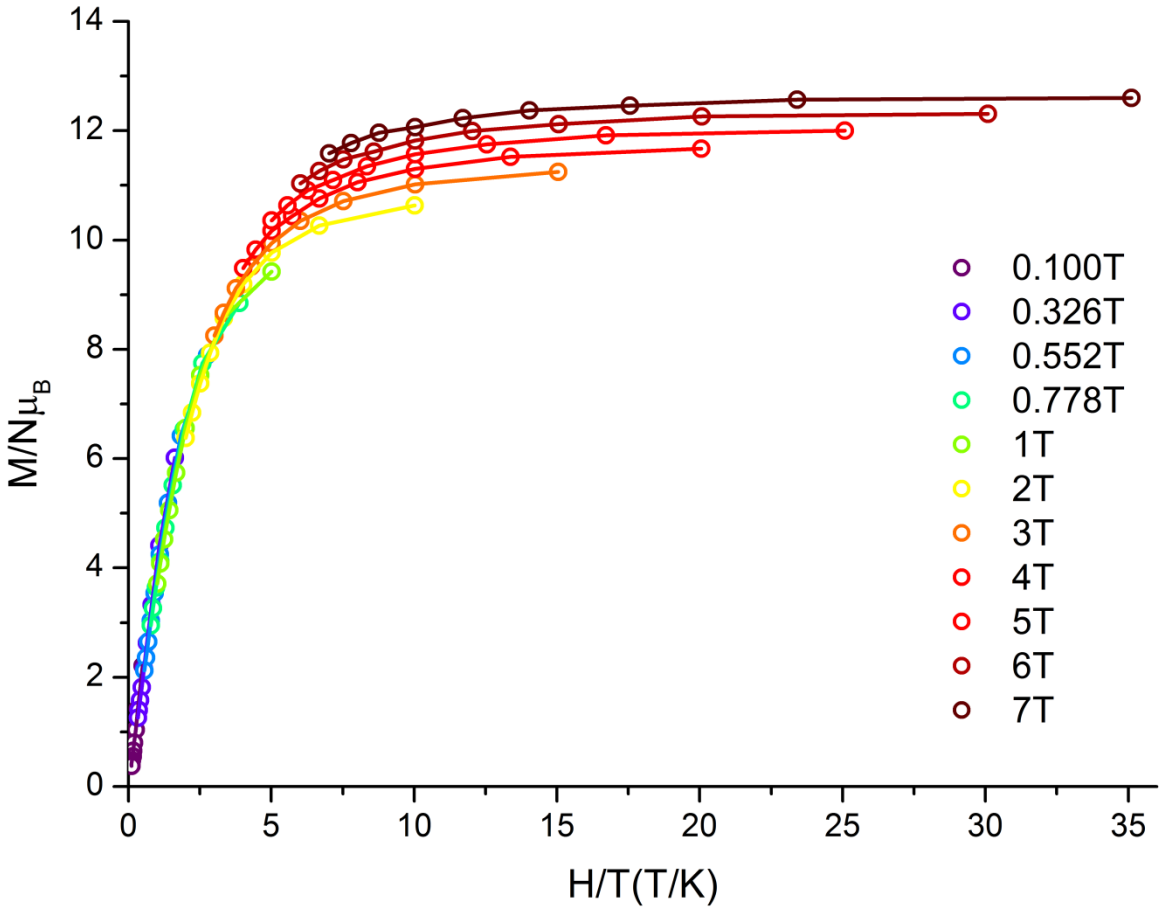

Figure S23 Field-temperature ratio dependence of the reduced magnetization ($M/N\mu_B$ vs. H/T plot) of **1** at temperatures between 2 and 10 K for applied magnetic fields from 0.1 to 7 T; the solid lines are guidelines for the eyes.

References

1 A.L. Spek, *Acta Cryst.*, 2009, **D65**, 148.

2 R.H. Blessing, *Acta Cryst.*, 1995, **A51**, 33.

3 A. Altomare, M.C. Burla, M. Camalli, G.L. Cascarano, C. Giacovazzo, A. Guagliardi et al., *J. Appl. Cryst.*, 1999, **32**, 115.

4 G.M. Sheldrick, *Acta Cryst.*, 2008, ***A*64**, 112.

5 C. Dendrinou-Samara, G. Psomas, L. Iordanidis, V. Tangoulis and D.P. Kessissoglou, *Chem. Eur. J.*, 2001, **7**, 5041.

6 G. Psomas, A.J. Stemmler, C. Dendrinou-Samara, J.J. Bodwin, M. Schneider, M. Alexiou et al., *Inorg. Chem.*, 2001, **40**, 1562.

7 D.P. Kessissoglou, J.J. Bodwin, J. Kampf, C. Dendrinou-Samara and V.L. Pecoraro, *Inorg. Chim. Acta*, 2002, **331**, 73.

8 C. Dendrinou-Samara, L. Alevizopoulou, L. Iordanidis, E. Samaras and D.P. Kessissoglou, *J. Inorg. Biochem.*, 2002, **89**, 89.

9 M. Alexiou, I. Tsivikas, C. Dendrinou-Samara, A.A. Pantazaki, P. Trikalitis, N. Lalioti et al., *J. Inorg. Biochem.*, 2003, **93**, 256.

10 C. Dendrinou-Samara, A.N. Papadopoulos, D.A. Malamatari, A. Tarushi, C.P. Raptopoulou, A. Terzis et al., *J. Inorg. Biochem.*, 2005, **99**, 864.

11 B.R. Gibney, D.P. Kessissoglou, J.W. Kampf and V.L. Pecoraro, *Inorg. Chem.*, 1994, **33**, 4840.

12 E. Farkas, E. Kozma, M. Petho, K.M. Herlihy and G. Micera, *Polyhedron*, 1998, **17**, 3331.

13 C. Mulcahy, K.A. Krot, D.M. Griffith, K.Yu Suponitsky, Z.A. Starikova and C.J. Marmion, *Eur. J. Inorg. Chem.*, 2007, **2007**, 1373.

14 E. Farkas, D. Bátka, H. Csóka and N.V. Nagy, *Bioinorg. Chem. Appl.*, 2007, **2007**, 1.

15 S. Dhungana, J.M. Harrington, P. Gebhardt, U. Möllmann and A.L. Crumbliss, *Inorg. Chem.*, 2007, **46**, 8362.

16 K. Lagarec and D. Rancourt, *Nucl. Instr. Meth. Phys. Res. B*, 1997, **129**, 266.

17 G.A. Bain and J.F. Berry, *J. Chem. Educ.*, 2008, **85**, 532.

18 D. Gatteschi and L. Pardi, *Gazz. Chim. Ital.*, 1993, 231.

19 L. Engelhardt, S.C. Garland, C. Rainey and R.A. Freeman, **2013**, *arXiv:1305.0238 [cond-mat.str-el]*.